

# Chemical Science

Accepted Manuscript

This article can be cited before page numbers have been issued, to do this please use: W. Zhang and X. Ning, *Chem. Sci.*, 2026, DOI: 10.1039/D6SC03818B.



This is an Accepted Manuscript, which has been through the Royal Society of Chemistry peer review process and has been accepted for publication.

Accepted Manuscripts are published online shortly after acceptance, before technical editing, formatting and proof reading. Using this free service, authors can make their results available to the community, in citable form, before we publish the edited article. We will replace this Accepted Manuscript with the edited and formatted Advance Article as soon as it is available.

You can find more information about Accepted Manuscripts in the [Information for Authors](#).

Please note that technical editing may introduce minor changes to the text and/or graphics, which may alter content. The journal's standard [Terms & Conditions](#) and the [Ethical guidelines](#) still apply. In no event shall the Royal Society of Chemistry be held responsible for any errors or omissions in this Accepted Manuscript or any consequences arising from the use of any information it contains.

# Role of the Fe-FeCl<sub>2</sub> Contact Interface in Promoting Redox Reversibility and Electrochemical Kinetics in Fe/FeCl<sub>2</sub>-Graphite Molten Salt Battery

Wenlong Zhang, Xiaohui Ning\*

## Author Address

Wenlong Zhang-Center for Alloy Innovation and Design (CAID), State Key Laboratory for Mechanical Behavior of Materials, Xi'an Jiaotong University, Xi'an, Shaanxi 710049, P. R. China.

Xiaohui Ning-Center for Alloy Innovation and Design (CAID), State Key Laboratory for Mechanical Behavior of Materials, Xi'an Jiaotong University, Xi'an, Shaanxi 710049, P. R. China. Email: xiaohuining@mail.xjtu.edu.cn

## Keywords

Fe-FeCl<sub>2</sub> interface; Dry powder calendaring; Fe/FeCl<sub>2</sub>-Graphite battery; Intermediate temperature molten salt battery

## Abstract

The Fe/FeCl<sub>2</sub>-Graphite battery is an intermediate-temperature molten salt electrochemical system. It employs the solid Fe/Fe<sup>2+</sup> redox as the negative electrode reactions and graphite positive electrode based on the intercalation/de-intercalation reaction of AlCl<sub>4</sub><sup>-</sup>, offering high safety, low material cost and a moderate operating temperature range of 110-150 °C. However, the poor electronic conductivity and high nucleation barrier in the FeCl<sub>2</sub> material result in limited electrochemical reversibility



and reaction kinetics. Here, we demonstrate that the Fe-FeCl<sub>2</sub> contact interface effectively enhances the redox reversibility and electrode kinetics by providing favorable sites for Fe<sup>0</sup> nucleation and improving electronic conductivity. The prepared Fe-FeCl<sub>2</sub>-CR electrode delivers low voltage hysteresis of 0.09 V and exhibits excellent electrochemical reversibility in the Fe/FeCl<sub>2</sub>-graphite molten salt battery, achieving a specific capacity of 162.6 mAh g<sup>-1</sup> at 3 mA cm<sup>-2</sup> and retaining 93% of its capacity after 200 cycles. Compared with the pure FeCl<sub>2</sub> electrode, the Fe-FeCl<sub>2</sub>-CR electrode shows lower direct-current pulse resistance and negligible nucleation overpotential, which are primarily attributed to the Fe-philic nucleation interface. This mechanism is further confirmed by density functional theory (DFT) calculations, revealing that the (110) crystal plane of nano-Fe possesses the highest binding energy (-55.94 eV) during charging, thereby serving as the potential dominant interface for Fe<sup>0</sup> nucleation. Additional self-discharge and capacity expansion tests further confirm the electrochemical reaction stability of Fe-FeCl<sub>2</sub>-CR electrode in Fe/FeCl<sub>2</sub>-Graphite molten salt battery.

## 1. Introduction

The global transition toward renewable and sustainable energy has accelerated the need for advanced large-scale electrical energy storage technologies to support the integration of intermittent clean energy sources. Driven by market demands, the evolution of rechargeable battery-based large-scale storage systems imposes increasingly stringent requirements on cost-effectiveness, safety, and cycle life<sup>1</sup>. There is an urgent need to develop highly reversible electrochemical systems with intrinsically



safe electrode and electrolyte materials. Molten salt batteries utilizing inorganic ionic liquids offer distinct advantages in terms of electrode reaction kinetics, electrolyte safety, and ionic conductivity<sup>2</sup>. For instance, novel low melting point molten salt electrode materials (NMPV, SMS-FeX<sub>3</sub>, QASs-NMP etc.) formed by the complexation coordination of metallic/non-metallic ion (Fe<sup>3+</sup>, V<sup>3+</sup>, Co<sup>2+</sup>, quaternary ammonium salts etc.) with the lone pair electrons of N-methyl pyrrolidone (NMP) were found to exhibit excellent electronic conductivity and electrochemical activity, and demonstrate high lithium-ion storage capacity and stable electrode reactions<sup>3-6</sup>. Owing to their unique three-layer liquid electrode/electrolyte structure, the rapid electron/ion exchange at the liquid metal/ionic liquid interface endows liquid metal batteries with excellent power density, enabling operation at high current densities up to 1250 mA cm<sup>-2</sup><sup>7</sup>.

Leveraging the stable chemical properties of Na<sup>+</sup>-conducting solid electrolytes (e.g.,  $\beta$ -Al<sub>2</sub>O<sub>3</sub>) and the high electrode potential of metal chloride electrodes (e.g. NiCl<sub>2</sub>, FeCl<sub>2</sub>, ZnCl<sub>2</sub>), sodium-metal chloride batteries demonstrate high discharge voltage and good electrochemical activity within a medium-temperature range of 150-200 °C<sup>8, 9</sup>. Furthermore, the intercalation/de-intercalation of AlCl<sub>4</sub><sup>-</sup> anions into graphite interlayers has been shown to exhibit outstanding electrochemical reversibility in aluminum-ion batteries, both in room-temperature ionic liquid electrolytes and inorganic molten salt electrolytes. For example, a 3D graphite foam positive electrode showed nearly negligible capacity decay after 7500 cycles at high current density of 4 A g<sup>-1</sup> in an AlCl<sub>3</sub>/[EMIm]Cl ionic liquid electrolyte at room temperature<sup>10</sup>. Meanwhile, commercial graphite paper used as the positive electrode in aluminum-ion batteries has



also demonstrated a high specific capacity of 114.9 mAh g<sup>-1</sup> after 1,500 cycles (at 0.2 A g<sup>-1</sup>) in a quaternary low-melting-point molten salt electrolyte (AlCl<sub>3</sub>-NaCl-LiCl-KCl). Notably, the cost of such inorganic molten salt electrolytes is approximately one-sixth that of organic ionic liquid electrolytes (e.g., AlCl<sub>3</sub>/[EMIm]Cl with a molar ratio of 1.3)<sup>11</sup>.

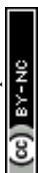
Focusing on lower operating temperatures and high-abundance electrode/electrolyte materials, a novel Fe/FeCl<sub>2</sub>-graphite molten salt battery was first proposed in 2019 by Ning et al, based on a NaAlCl<sub>4</sub> molten salt electrolyte at 170 °C. In this system, the positive and negative electrodes inherit the reaction mechanisms of the graphite electrode from aluminum-ion batteries and the metal chloride electrode from sodium–metal chloride batteries, respectively<sup>12, 13</sup>. During charging, the graphite positive electrode primarily undergoes the intercalation of AlCl<sub>4</sub> ions to form graphite intercalation compounds (GICs), while a reduction reaction occurs at the FeCl<sub>2</sub> negative electrode, generating solid metallic iron (Fe) and sodium chloride (NaCl). When paired with the Fe/FeCl<sub>2</sub> foam metal negative electrode, the graphite positive electrode delivered a specific capacity of approximately 104 mAh g<sup>-1</sup>, with 85% capacity retention after 10,000 cycles. Unlike the liquid deposition of Fe<sup>2+</sup> in iron-metal batteries or the solid-state oxidation of Fe in Na-FeCl<sub>2</sub> molten salt batteries, the initial active material in the fully discharged Fe/FeCl<sub>2</sub>-graphite battery is solely FeCl<sub>2</sub><sup>14</sup>. The poor electronic conductivity and high nucleation energy barrier for the FeCl<sub>2</sub> → Fe conversion are the main factors limiting the development of FeCl<sub>2</sub> negative electrode with high electrochemical reversibility. Previous studies have shown that fabricating

View Article Online  
DOI: 10.1039/D6SC03818B



FeCl<sub>2</sub> active material at an iron matrix interface can not only improve the electrical conductivity but also provide an Fe-philic nucleation interface for the reduction of FeCl<sub>2</sub>. For instance, Ning et al. investigated the electrochemical properties of FeCl<sub>2</sub>/Fe negative electrode synthesized via HCl gas-phase chemical chlorination and galvanostatic/potentiostatic electrochemical chlorination within an iron foam matrix. The Fe/FeCl<sub>2</sub>-EAE-1.4V electrode, prepared by galvanostatic electrochemical chlorination, exhibited lower electrochemical polarization and a higher areal capacity (0.72 mAh cm<sup>-2</sup> at 5.0 mA cm<sup>-2</sup> after 7,000 cycles) compared to the sample prepared by HCl gas-phase chlorination in the Fe/FeCl<sub>2</sub>-graphite molten salt battery<sup>15</sup>. Similarly, Wu et al studied the Fe<sup>2+</sup>/Fe<sup>0</sup> redox couple in an AlCl<sub>3</sub>/[EMIm]Cl ionic liquid electrolyte using an iron foil positive electrode and an aluminum negative electrode<sup>16</sup>. Their results indicated that at appropriate current densities (0.2 mA cm<sup>-2</sup>), a 304-type austenitic stainless-steel foil (50 μm thick) used as an Fe nucleation interface in an Al-Fe battery achieved Coulombic efficiency of 99% and areal capacity of 0.74 mAh cm<sup>-2</sup>. However, whether in foam metal or foil electrodes, Fe atoms within the bulk material have limited participation in surface electrode reactions, leading to low active material utilization and constrained electrode energy density. Therefore, designing FeCl<sub>2</sub> negative electrode preparation strategies that maximize the Fe-FeCl<sub>2</sub> contact interface is an effective approach to developing high-energy-density Fe/FeCl<sub>2</sub>-graphite molten salt battery.

In this work, we designed the Fe-FeCl<sub>2</sub> contact interface via the direct dry-powder calendaring process. A substantial Fe-FeCl<sub>2</sub> contact interface is achieved by ball



milling nano-Fe powder with  $\text{FeCl}_2$  powder, which effectively enhanced the redox electrochemical activity of the Fe/ $\text{FeCl}_2$  negative electrode. The nano-Fe powder not only serves as an Fe-philic nucleation interface to guide the distribution of the reduction product ( $\text{Fe}^0$ ) but also significantly improves the electronic conductivity of the composite electrode.  $\text{FeCl}_2$  are used as the starting active material to meet the assembly requirements of the fully discharged initial state. First, we investigated the effect of nano-Fe powder addition on electrochemical performance under different active material ratios in Fe/ $\text{FeCl}_2$ -graphite full cells. Results shows that the Fe- $\text{FeCl}_2$ -CR-60 electrode delivered the specific capacity of  $162.6 \text{ mAh g}^{-1}$  at  $3 \text{ mA cm}^{-2}$  and retained 93% of its capacity after 200 cycles, with active material utilization increasing to 27.15%. Second, we examined the electrochemical interface characteristics of electrodes containing nano-Fe powder using Al-Fe half-cells and the three-electrode system. Compared to the pure  $\text{FeCl}_2$  electrode, the Fe- $\text{FeCl}_2$ -CR-60 electrode exhibited low redox overpotential of 90 mV and a DC pulse resistance of  $1.74 \Omega$ , confirming high electrochemical reversibility and low nucleation energy barrier at the Fe- $\text{FeCl}_2$  interface. Finally, reaction mechanism analysis of the Fe- $\text{FeCl}_2$ -CR-60 electrode indicated that the full-cell charging process corresponds to the conversion of  $\text{FeCl}_2$  to  $\text{Fe}^0$  and crystalline NaCl, and the surface of the added nano-Fe powder gradually transforms into active interface during cycling. Furthermore, Fe/ $\text{FeCl}_2$ -graphite full cells assembled with Fe- $\text{FeCl}_2$ -CR-60 negative electrodes exhibited low self-discharge (retaining the initial discharge capacity of  $196.7 \text{ mAh g}^{-1}$  after 168 hours of cooling storage) and good scalability (electrode area =  $11.3 \text{ cm}^2$ , initial electrode capacity = 13



mAh). This Fe-FeCl<sub>2</sub> contact interface provides valuable insights for the future large-scale development of intermediate-temperature Fe/FeCl<sub>2</sub>-graphite molten salt battery.

## 2. Material and methods

### 2.1. Preparation of molten salt electrolyte

The preparation of the molten salt electrolyte primarily involves dehydration heating and pre-melting under the Ar atmosphere. NaCl (99.5%, Aladdin), AlCl<sub>3</sub> (99%, Aladdin), and LiCl (99%, Aladdin) are first subjected to the preliminary dehydration treatment in a resistance furnace. Given its low melting point (194 °C) and sublimation temperature (183 °C), AlCl<sub>3</sub> is pretreated at 80 °C for 12 h. The remaining salts, LiCl and NaCl, are heated separately at 80 °C and 250 °C for 12 h, respectively. After dehydration, the salts are mixed in the molar ratio of AlCl<sub>3</sub>:LiCl:NaCl = 2:1:1. The resulting ternary electrolyte has a melting point of approximately 105 °C; therefore, the mixed salts are pre-melted at 200 °C for 12 h and then at 150 °C for 24 h. During this stage, high-purity aluminum strips are added to remove impurities from the melt until the electrolyte became transparent. After the pre-melting process, the molten salt electrolyte is allowed to cool naturally, and the resulting solid white blocks are ground and collected.

### 2.2 Preparation of Fe-FeCl<sub>2</sub>-CR electrode

The preparation of Fe-FeCl<sub>2</sub>-CR electrodes are carried out by dry powder roll-to-rolled calendaring. Firstly, anhydrous FeCl<sub>2</sub> (99.5%, Aladdin) was ball milled at 500 r/min for 6 hours at Ar gas atmosphere. Secondly, the obtained anhydrous FeCl<sub>2</sub> are uniformly mixed with acetylene black (AB, 99.9%, Alfa Aesar), polytetrafluoroethylene



(PTEF, Aladdin) and nano Fe powder (50 nm, 99.9%, Macklin) in mass ratio of FeCl<sub>2</sub> + Fe: AB: PTEF = 40:30: 30 wt%. The mixed materials are rolled repeatedly by using the electric roller machine (MSK-2150, KEJING STAR Technology Co., Ltd) until the thickness of electrode material is about 10 μm, and the active substance loading is 6-8 mg/cm<sup>2</sup>. Due to the electrochemical activity of nano-Fe powder, all electrode specific capacity calculations are based on the total mass of Fe + FeCl<sub>2</sub>. In all three-electrode tests, the metal molybdenum (Mo) mesh was used as the electrode current collector for fixation. Finally, the calendaring electrode was cut into discs with diameter of 10 mm. All obtained electrodes were kept at 250 °C for 12 hours in Ar atmosphere for cross-linking and moisture remove. To investigate the electrochemical reaction laws of nano-Fe and FeCl<sub>2</sub>, electrodes with different contents and material ratios (0, 20, 40, 60, 80 and 100 wt%) are prepared and named as (Fe-CR, Fe-FeCl<sub>2</sub>-CR-xx and FeCl<sub>2</sub>-CR) according to the same steps.

### 2.3. Electrochemical measurements

The structure of the testing batteries is referred to our previous research literatures<sup>17</sup>. Firstly, the pre-melted electrolyte is placed in a quartz crucible and remelted at 150 °C. Appropriate molten salt electrolyte is added to the internal cavities of the positive and negative electrodes, in which the melted electrolyte acts as separator to prevent short circuit. Due to the low viscosity and excellent fluidity, the electrolyte fully wet the surfaces of the positive and negative electrodes. After the molten electrolyte solidified, molybdenum foil current collectors (50 μm, 99.99%) are placed contact with graphite positive electrode (0.1 mm, Shandong Huatai graphite) and



calendering Fe/FeCl<sub>2</sub> negative electrode respectively. Finally, the stainless-steel shells are placed contact with the molybdenum foil and fixed by the nut clamps. All the above operations are carried out in a glove box filled with Ar, under O<sub>2</sub> < 1.0 ppm and H<sub>2</sub>O < 1.0 ppm. The assembled batteries are tested at 130 °C in air. The galvanostatic charging and discharging tests are mainly conducted by using Neware battery tester (CT-4008T-5V10MA), while the test of capacity expanded batteries and pulse resistance are performed by applying an Arbin BT2000 instrument. For all the three-electrode tests, aluminum foil (100 μm, 99.999%) is used as the reference electrode and counter electrode. The corresponding cyclic voltammetry is carried out by using an electrochemical workstation (Autolab-PGSTAT204, Metrohm).

## 2.4 Material characterization

X-ray powder diffraction (XRD, X'Pert PRO, PANalytical B.V.) is employed to detect the composition and structural changes of electrode materials. Scanning electron microscopy (SEM, SU6600, Japan) and EDX energy-dispersive spectroscopy are utilized to observe the morphology and surface elements of the electrode materials, with an accelerating voltage of 15 kV and working distance of 10 mm. To explore the variation of the graphite carbon atoms vibration state before and after the charging process, Raman spectroscopy (DXR3xi, Thermo Fisher Scientific) is adopted to detect the graphite material in initial state and the fully charged state, with laser wavelength of 532 nm and power of 3.2%.

## 2.5 Calculation method

Density functional theory as implemented in the Vienna Ab-initio Simulation



Package (VASP)<sup>18, 19</sup> is employed to optimize geometry structures. The exchange-correlation interactions are described by the generalized gradient approximation (GGA) in the form of the Perdew-Burke-Ernzerhof functional (PBE)<sup>20</sup>. We have chosen the projected augmented wave (PAW) potentials<sup>21, 22</sup> to describe the ionic cores and take valence electrons into account using a plane wave basis set with a kinetic energy cutoff of 450 eV. The electronic energy is considered self-consistent when the energy change is smaller than  $10^{-5}$  eV. A geometry optimization is considered convergent when the force change is smaller than 0.04 eV/Å. The vacuum spacing in a direction perpendicular to the plane of the structure is 15 Å. The van der Waals interactions are considered by the method of the Grimme (DFT+D3)<sup>23</sup>. The Brillouin-zone integration is sampled with a Monkhorst-Pack mesh of  $2 \times 2 \times 1$  in the structural relaxation calculations. The binding energy is presented by the formula:

$$E_{\text{bind}} = E_{\text{substrate+mol}} - E_{\text{substrate}} - E_{\text{mol}}$$

where  $E_{\text{substrate+mol}}$  is the total energy of substrate with adsorbed molecules,  $E_{\text{substrate}}$  is the energy of clean surface of slab model,  $E_{\text{mol}}$  is the energy of single molecule in gas phase.

### 3. Results and discussion



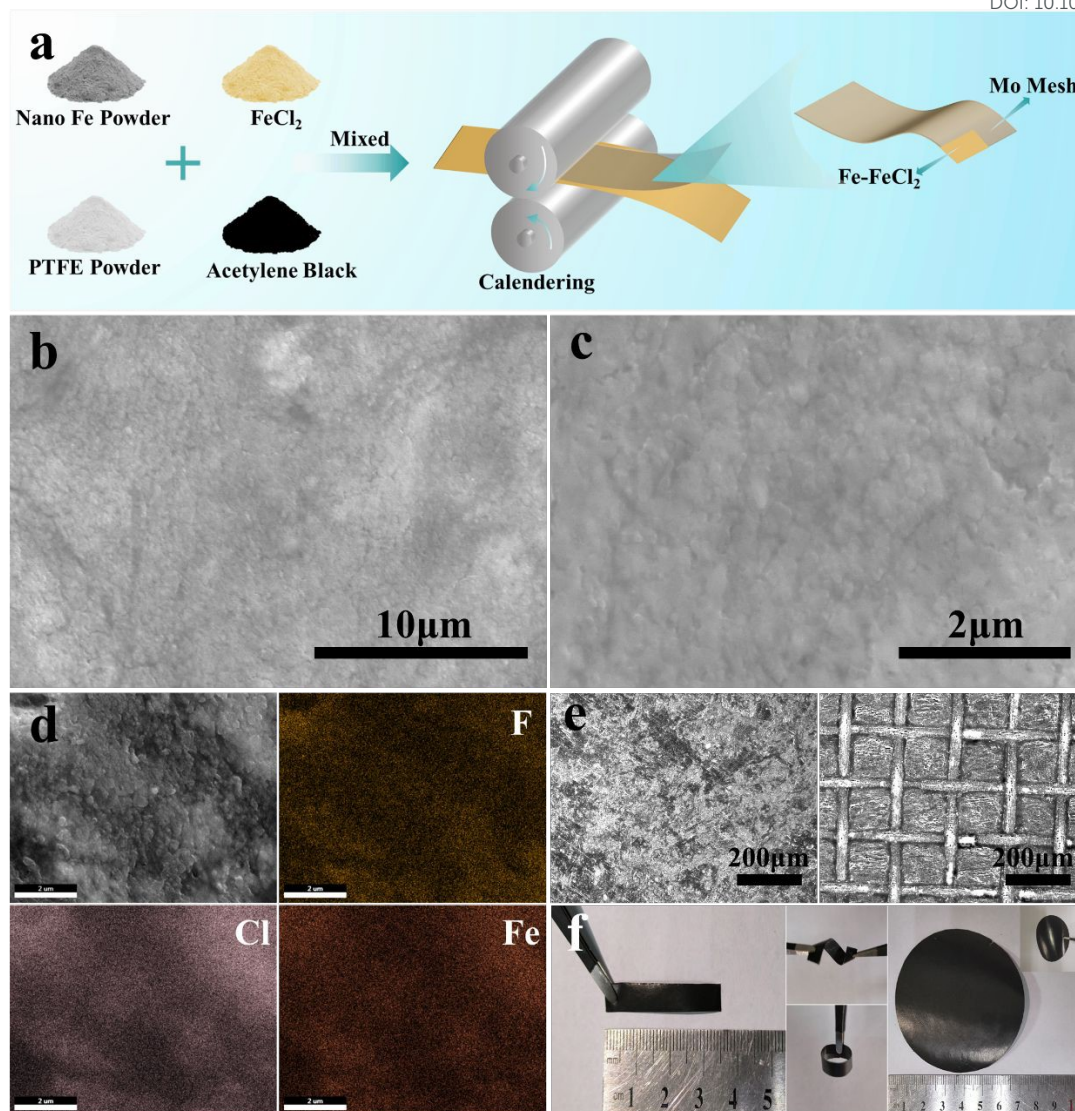
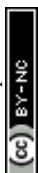


**Figure 1.** (a) Preparation diagram of the dry powder calendaring Fe/FeCl<sub>2</sub>-CR electrode. (b-c) SEM images of the Fe/FeCl<sub>2</sub>-CR electrode surface. (d) SEM-EDS elemental mapping images of the Fe/FeCl<sub>2</sub>-CR electrode. (e-f) Both sides optical images of Fe/FeCl<sub>2</sub>-CR electrode embedded with molybdenum mesh.

In the Fe/FeCl<sub>2</sub>-graphite molten salt battery, the electrochemical reversibility and energy density of the Fe<sup>2+</sup>/Fe<sup>0</sup> redox couple are limited by the accessible Fe/FeCl<sub>2</sub> interface at the electrolyte. Electrode preparation methods based on the chemical or electrochemical surface oxidation of Fe matrix struggle to ensure sufficient electrode

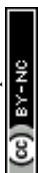


reaction sites within the Fe bulk. Moreover, the aggressive ionic environment of molten salt electrolytes compromises the chemical stability of electrodes fabricated by conventional slurry-casting processes. Here, Fe-FeCl<sub>2</sub>-CR electrodes are fabricated using the chemically stable binder polytetrafluoroethylene (PTFE). As illustrated in **Figure 1a**, after ball milling, nano-Fe and FeCl<sub>2</sub> powders are repeatedly calendered with the binder and conductive additive (acetylene black) to produce the freestanding Fe-FeCl<sub>2</sub>-CR electrode with uniform bulk composition<sup>24</sup>. To enhance electronic conductivity in three-electrode tests and large-area cells, a molybdenum mesh (75 μm aperture) is calendered into the interior of the Fe-FeCl<sub>2</sub>-CR electrode to serve as the integrated current collector. Prior to testing, all electrodes are heat-treated at 250 °C under the Ar atmosphere to promote intermolecular cross-linking of the binder and remove residual moisture<sup>25</sup>. **Figure 1b-c** reveal different magnification SEM images of the calendering Fe-FeCl<sub>2</sub>-CR electrode, in which the low-magnification image shows the uniform granular composition without cracks or voids. **Figure 1c** further demonstrates that the Fe-FeCl<sub>2</sub>-CR electrode surface primarily consists of PTFE-encapsulated granular materials, with active substances (nano Fe powder and FeCl<sub>2</sub> powder) homogeneously dispersed. Combining the corresponding SEM-EDS images in **Figure 1d**, it can be observed that the Fe-FeCl<sub>2</sub>-CR electrode surface is mainly composed of F (PTFE), Cl (FeCl<sub>2</sub>), and Fe (Fe or FeCl<sub>2</sub>) elements, confirming the excellent material uniformity in the Fe-FeCl<sub>2</sub>-CR electrode prepared by calendering process. **Figure 1e** presents both sides optical images of Fe-FeCl<sub>2</sub>-CR electrode with molybdenum mesh embedding. Profit by the excellent ductility and adhesion ability of PTFE, Fe-FeCl<sub>2</sub>-CR electrode



three-electrode system embedded with molybdenum mesh exhibits superior mechanical strength and toughness. 360° bending and twisting in **Figure 1f** further confirms the excellent flexibility and mechanical strength of Fe-FeCl<sub>2</sub>-CR electrode. The preparation of Fe-FeCl<sub>2</sub>-CR electrode with expanded area (11.3 cm<sup>2</sup>) demonstrates the feasibility of this dry powder process strategy in large-scale practical applications.

The Fe/FeCl<sub>2</sub>-graphite molten salt battery operates in the AlCl<sub>3</sub>/LiCl/NaCl ternary inorganic molten salt electrolyte. As shown in **Figure 2a**, during charging, the FeCl<sub>2</sub> negative electrode is reduced to metallic Fe<sup>0</sup> and NaCl, while the graphite positive electrode undergoes the intercalation of AlCl<sub>4</sub><sup>-</sup> anions into its layers, forming the corresponding graphite intercalation compounds. The discharge process corresponds to the reverse reactions.<sup>12, 15</sup> In practice, the battery is assembled in the fully discharged state, with FeCl<sub>2</sub> and pristine graphite paper serving as the active materials for the negative and positive electrodes, respectively. To examine the material properties of the dry powder calendered FeCl<sub>2</sub>-CR electrode, **Figure 2b-c** present its XRD pattern and Raman spectrum. The XRD pattern shows clear diffraction peaks corresponding to crystalline FeCl<sub>2</sub> (PDF#01-1106) and PTFE (PDF#47-2217). In the Raman spectrum, the peaks at 1353 cm<sup>-1</sup> and 1597 cm<sup>-1</sup> originate from the D and G bands of sp<sup>2</sup>-hybridized carbon in the acetylene black, while the peak at 229 cm<sup>-1</sup> is characteristic of FeCl<sub>2</sub> in the electrode.



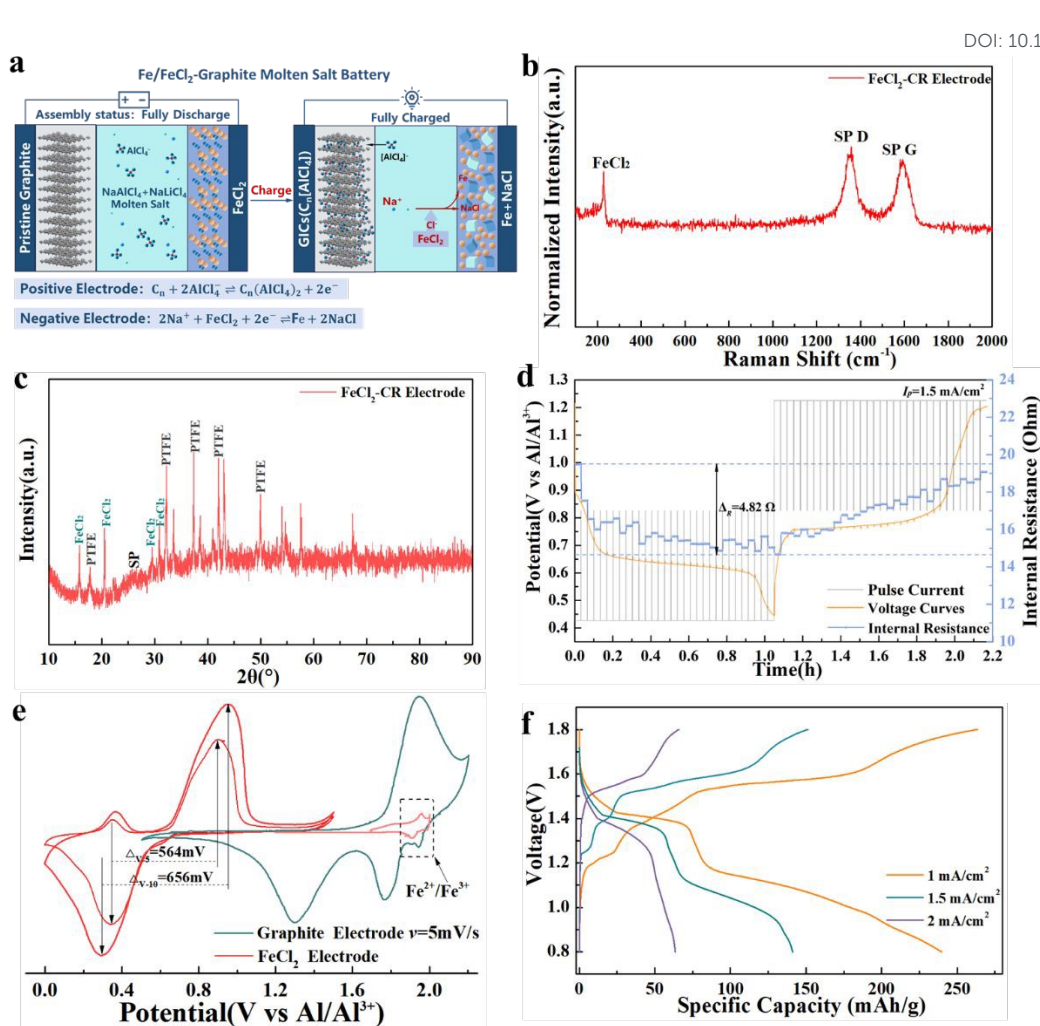
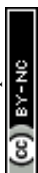


**Figure 2.** (a) Preparation diagram of the Fe/FeCl<sub>2</sub>-graphite molten salt battery. (b) Raman spectrum of the FeCl<sub>2</sub>-CR electrode. (c) XRD pattern of the FeCl<sub>2</sub>-CR electrode. (d) DC pulse resistance measurements of FeCl<sub>2</sub>-CR electrode in the Al-FeCl<sub>2</sub> half-cell during charge/discharge. (e) Cyclic voltammetry curves of the FeCl<sub>2</sub>-CR electrode and graphite electrode at different scan rates in the three-electrode system. (f) Voltage profiles of the Fe/FeCl<sub>2</sub>-graphite molten salt battery at varied current densities.

To compare the electronic conductivity of FeCl<sub>2</sub> and its reduction product (Fe<sup>0</sup>), DC pulse-resistance measurements (pulse duration: 0.5 s) were performed on an Al-FeCl<sub>2</sub> half-cell to monitor the internal resistance changes during reduction and oxidation. As shown in **Figure 2d**, the internal resistance decreases from 19.48 Ω



(FeCl<sub>2</sub> phase) to 14.66 Ω (Fe + NaCl phase) during discharge, corresponding to the resistance drop of ΔR = 4.82 Ω, which is primarily attributed to the higher electronic conductivity of metallic Fe compared to FeCl<sub>2</sub>. To investigate the electrochemical window of the molten salt electrolyte, we performed CV tests by using metallic gold (Au) as the working electrode. As shown in **Figure S2**, the Au electrode exhibited two extreme electrochemical reactions at a scan rate of 10 mV/s, corresponding to the evolution of chlorine gas and the deposition/dissolution reaction of metallic aluminum at 2.2 V and -0.04 V, respectively. This is close to the electrochemical window of similar molten salt electrolytes (AlCl<sub>3</sub>/NaCl) (approximately 0-2.2 V, vs Al/Al<sup>3+</sup>)<sup>26, 27</sup>. To explore the electrochemical behavior of the pure FeCl<sub>2</sub> electrode and graphite paper electrode, cyclic voltammetry was carried out in the three-electrode configuration using metallic aluminum as both the reference and counter electrode, within the potential window of 0-2.2 V (test setup shown in **Figure S1**). When the scan rate is increased from 5 to 10 mV s<sup>-1</sup>, the FeCl<sub>2</sub>-CR electrode displayed reduction and oxidation peaks near 0.3 V and 0.9 V, corresponding to the Fe<sup>2+</sup>/Fe<sup>0</sup> redox couple, consistent with the reported electrode potentials of FeCl<sub>2</sub> in ionic-liquid electrolytes.<sup>16</sup>

In the AlCl<sub>3</sub>-NaCl-LiCl electrolyte, the redox behavior of the FeCl<sub>2</sub>-CR electrode (Fe<sup>2+</sup>/Fe<sup>0</sup>) and the graphite electrode (C□/C□[AlCl<sub>4</sub>]) is further characterized within the potential range of 1.2-2.0 V. The results show that the oxidation and reduction reactions of FeCl<sub>2</sub> proceed within the potential window of AlCl<sub>4</sub> intercalation/deintercalation into graphite, confirming the absence of significant high-potential side reactions at the FeCl<sub>2</sub>-CR electrode during the operation of the



Fe/FeCl<sub>2</sub>-graphite full cell. The peak separation (in **Figure 2e**) between oxidation and reduction potentials increases from 564 mV to 656 mV as the scan rate increasing, indicating sluggish reaction kinetics inherent to the bulk FeCl<sub>2</sub> material. The voltage profiles and cycling performance of the FeCl<sub>2</sub>-CR electrode in the full-cell configuration are presented in **Figure 2f** and **Figure S4**. The electrode delivers discharge specific capacities of 239.7, 141.2, and 63.5 mAh g<sup>-1</sup> at current densities of 1, 1.5, and 2 mA cm<sup>-2</sup>, respectively. The poor capacity retention at higher current densities is likely due to high nucleation energy barriers and significant internal resistance differences. Furthermore, the distinct charge/discharge plateaus nearly vanish at 2 mA cm<sup>-2</sup> upon cycling, suggesting that metallic Fe<sup>0</sup> formed from the reduction of pure FeCl<sub>2</sub> cannot be fully re-oxidized in the subsequent charging step, leading to limited reversibility.

Based on the electrochemical behavior of the pure FeCl<sub>2</sub>-CR electrode and prior observations, the lack of compatible Fe<sup>0</sup> nucleation interface on pristine FeCl<sub>2</sub> is likely the main reason for its poor reversibility and sluggish kinetics. As illustrated in **Figure 3a-b**, the high nucleation energy barrier and lattice mismatch of bulk FeCl<sub>2</sub> can cause the reduction product (Fe<sup>0</sup>) to aggregate into clusters, resulting in the discontinuous and inefficient active interface. To provide compatible nucleation sites for Fe<sup>0</sup> and lower the interfacial energy barrier, we introduced nano-Fe powder as the pre-formed Fe interface to construct a continuous and stable reduction interface. As shown in **Figure S5-S10**, the cycling performance of Fe-FeCl<sub>2</sub>-CR electrodes with different nano-Fe contents was evaluated in full-cell configuration. The



Fe-FeCl<sub>2</sub>-CR-60 electrode (with 60 wt% nano-Fe) exhibited the best capacity retention and electrochemical stability. A comprehensive analysis (**Figure S11**) reveals that this electrode achieves the highest active-material utilization (27.15%) and the average specific capacity of 172.28 mAh g<sup>-1</sup>, along with the smallest capacity fluctuation (-0.04 mAh g<sup>-1</sup> cycle<sup>-1</sup>) over 100 cycles.

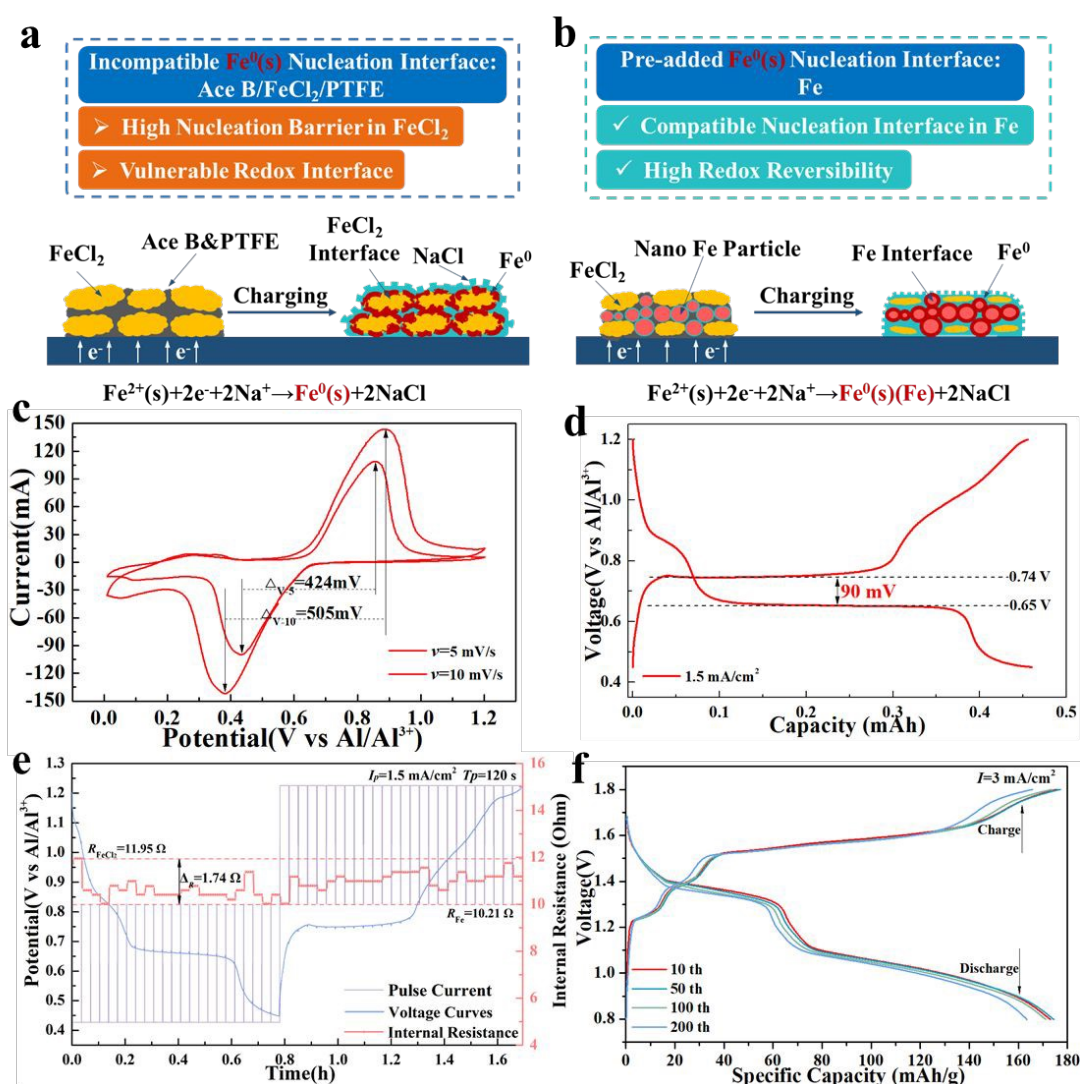
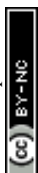


**Figure 3.** (a-b) Schematic illustration of the interface reduction mechanism at the FeCl<sub>2</sub>-CR electrode and the Fe-FeCl<sub>2</sub>-CR electrode. (c) Cyclic voltammetry curves of Fe-FeCl<sub>2</sub>-CR electrode at varied scan rates. (d) Charge/discharge profiles of the Fe-FeCl<sub>2</sub>-CR electrode in the Al-Fe/FeCl<sub>2</sub> half-cell. (e) DC pulse resistance testing of the



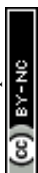
Fe-FeCl<sub>2</sub>-CR electrode. (f) Cycling performance of the Fe-FeCl<sub>2</sub>-CR electrode in Fe/FeCl<sub>2</sub>-graphite molten salt battery.

View Article Online  
DOI: 10.1039/D6SC03818B

Notably, electrodes with nano-Fe contents below 60 wt% show gradual capacity decay during cycling, whereas those with nano-Fe above 60 wt% display the capacity increase, which may be attributed to the initial activation of the nano-Fe interface. Similar activation behavior, involving the displacement of the subsurface passivation layer on nano-Fe, has been reported in Na-NiCl<sub>2</sub> molten-salt battery<sup>28,29</sup>. Therefore, we systematically investigated the electrochemical properties of the optimized Fe-FeCl<sub>2</sub>-CR-60 electrode in both three-electrode and Al-FeCl<sub>2</sub> half-cell setups. **Figure S3** and **Figure 3c** present the CV curves at different scan rates (5 mV/s, 10 mV/s, 15 mV/s and 20 mV/s) of Fe-FeCl<sub>2</sub>-CR-60 electrode under the same conditions. The oxidation/reduction polarization potentials of the electrode at the corresponding scan rates are 381 mV, 425 mV, 486 mV, and 549 mV, indicating that the oxidation/reduction reaction kinetics based on the Fe interface still needs further improvement. Additionally, the CV curves exhibited stable oxidation/reduction current peaks at different scan rates, demonstrating that the electrochemical reaction in the Fe-FeCl<sub>2</sub>-CR-60 electrode possess excellent electrode reversibility. Compared to the pure FeCl<sub>2</sub>-CR electrode (in **Figure 2e**), the pre-addition of nano-Fe reduces the polarization of the FeCl<sub>2</sub> bulk by 24.82% and 23.02% at these scan rates. The resulting Fe/Fe<sup>2+</sup> redox potentials (0.4-0.5 V for reduction, 1.0-1.1 V for oxidation vs. Al/Al<sup>3+</sup>) align well with those reported for the iron metal electrode in the Na-FeCl<sub>2</sub> molten-salt battery (NaAlCl<sub>4</sub> electrolyte at 190 °C).<sup>30</sup> In the Al-Fe/FeCl<sub>2</sub> half-cell, the voltage profiles of



the Fe-FeCl<sub>2</sub>-CR-60 electrode (**Figure 3d**) show clear charge and discharge plateaus at 0.74 V and 0.65 V, respectively, corresponding to the galvanostatic polarization voltage of only 90 mV. DC pulse-resistance measurements (**Figure 3e**) further reveal that the overall DC resistance of this electrode ranges from 10.21 to 11.95 Ω. The resistance difference between the oxidized and reduced states is reduced by 69.58% compared to the pure FeCl<sub>2</sub>-CR electrode, primarily due to the continuous conductive network provided by the nano-Fe particles. **Figure 3f** presents the stable voltage profile of the optimized Fe-FeCl<sub>2</sub>-CR-60 negative electrode during long-term cycling in the full-cell configuration. At a current density of 3.0 mA cm<sup>-2</sup>, the electrode delivers the specific capacity of 163.89 mAh g<sup>-1</sup> after 200 cycles, significantly higher than the 28.81 mAh g<sup>-1</sup> obtained with the pure FeCl<sub>2</sub>-CR negative electrode. **Figure S6** further confirms the electrochemical reversibility of the Fe-FeCl<sub>2</sub>-CR-60 electrode under moderate active mass loading (Fe+FeCl<sub>2</sub>:7.57 mg/cm<sup>2</sup>), the specific capacity of Fe-FeCl<sub>2</sub>-CR-60 electrode is 114.62 mAh/g after 200 cycles. In current research on metal chloride electrodes, similar cycling stability performance is acceptable. For example, Li et al developed a low-cost Na-FeCl<sub>2</sub> battery system based on the Fe/Fe<sup>2+</sup> redox reaction under operating conditions of 190 °C. By adding a small amount of metallic nickel powder (10 mol%), the corresponding Fe/Ni/NaCl electrode achieved an energy density of 295 Wh kg<sup>-1</sup> after 200 cycles ( $\approx C/5$ )<sup>30</sup>. Under the same operating temperature conditions, Wen et al developed a three-dimensional active Ni/NaCl electrode in the Na-NiCl<sub>2</sub> battery by using Ni-Carbon composite nanofiber as the matrix material. The continuous three-dimensional conductive network derived from electrospun fibers



effectively limits the growth of grain. And the NCCN-based electrode shows almost no capacity degradation after 350 cycles at  $2C^7$ .

View Article Online  
DOI: 10.1039/D6SC03818B

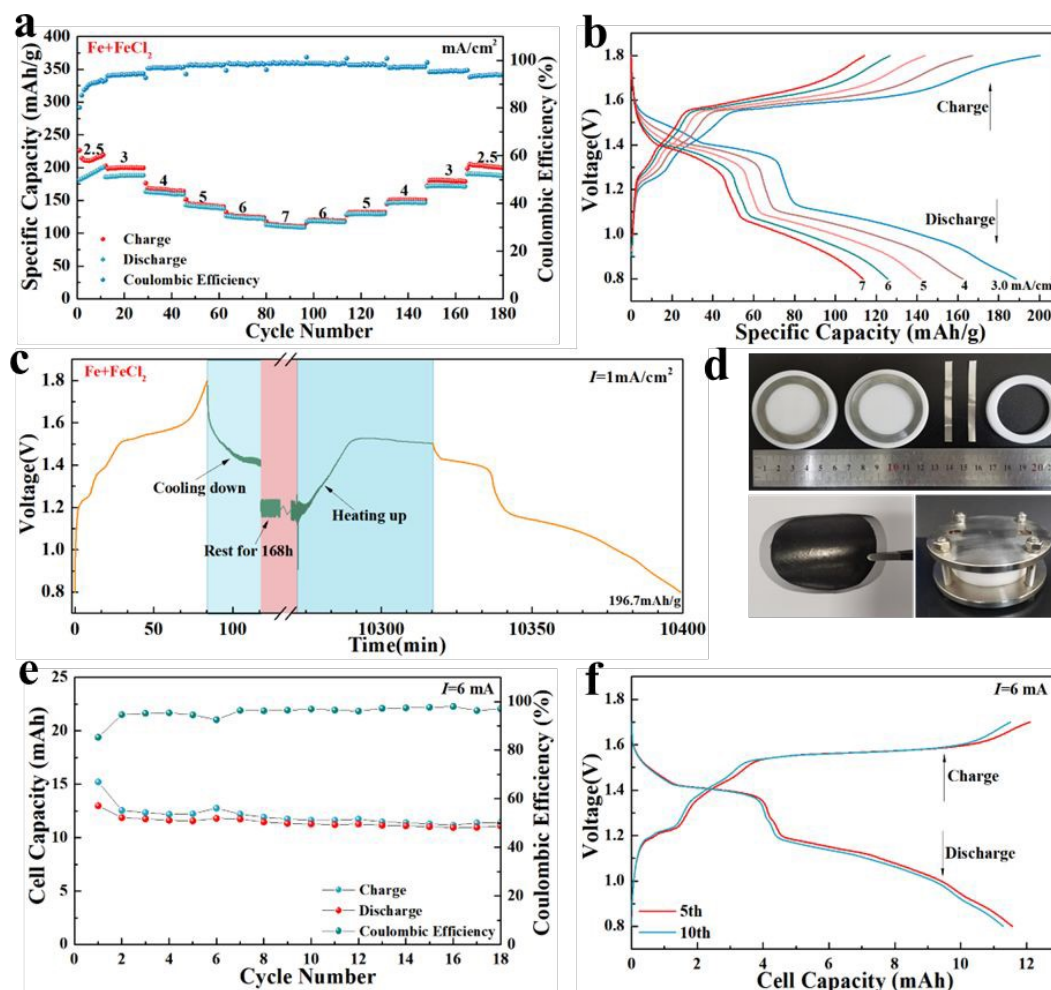


**Figure 4.** (a) Rate performance of the Fe-FeCl<sub>2</sub>-CR-60 electrode in Fe/FeCl<sub>2</sub>-graphite molten salt battery. (b) Corresponding voltage profiles at varied current densities. (c) Cooling storage characteristic of the Fe/FeCl<sub>2</sub>-Graphite molten salt battery. (d) Assembly images of Fe/FeCl<sub>2</sub>-Graphite molten salt battery with capacity expanded Fe-FeCl<sub>2</sub>-CR-60 negative electrode. (e-f) Cycling profile and voltage curves of capacity expanded Fe/FeCl<sub>2</sub>-graphite molten salt battery.

Building on the optimized reduction interface achieved by pre-adding nano-Fe to the FeCl<sub>2</sub> bulk, we conducted the comprehensive evaluation of the Fe-FeCl<sub>2</sub>-CR-60



electrode within the full Fe/FeCl<sub>2</sub>-graphite molten salt battery. As shown in **Figure 4a-b**, the electrode delivers specific capacities of 190.84, 187.55, 161.16, 140.13, 123.79, and 114.33 mAh g<sup>-1</sup> at current densities of 2.5, 3, 4, 5, 6, and 7 mA cm<sup>-2</sup>, respectively. When the current density is returned to 2.5 mA cm<sup>-2</sup>, the specific capacity recovers to 215.18 mAh g<sup>-1</sup>, demonstrating excellent rate capability and fast reaction kinetics. Owing to the insulating nature of the molten-salt electrolyte at room temperature, development fields with promising applications of these molten salt batteries are mainly including the thermoelectric combined scenarios, such as low-grade waste heat utilization and molten salt thermal storage power stations, in which it is suitable for long-term freeze-thaw reserve batteries and grid-level storage of seasonal by virtue of the solidification and insulation characteristics of molten salt electrolytes. Xu et al systematically demonstrated the application feasibility of molten salt batteries for seasonal energy storage in Al-Ni molten salt battery systems, achieving an effective capacity recovery of over 90% after 1–8 weeks of storage as a valid proof-of-concept verification<sup>31</sup>. Therefore, to assess their feasibility for room-temperature reserve applications, a fully charged Fe/FeCl<sub>2</sub>-graphite battery is cooled under natural conditions (**Figure 4c**) and rested at room temperature for one week before being discharged after temperature restoration. The results show nearly identical discharge voltage plateaus and the retained specific capacity of 196.7 mAh g<sup>-1</sup>, indicating excellent reserve characteristics and low self-discharge. Furthermore, to verify the electrochemical performance reliability of the Fe-FeCl<sub>2</sub>-CR-60 electrode prepared by the dry powder calendaring process, we extended the capacity of the Fe/FeCl<sub>2</sub>-graphite

test battery to greater than 10 mAh by simply expanding the electrode reaction area to 11.3 cm<sup>2</sup> (in **Figure 4d**). As shown in **Figure 4e-f**, the initial capacity of 13 mAh was obtained with an electrode area of 11.3 cm<sup>2</sup>, and the discharge capacity of 11.1 mAh is maintained after 18 cycles at the current of 6 mA, indicating that the Fe-FeCl<sub>2</sub>-CR-60 electrode with expanded active area still exhibit reversible electrode reactions. The charge/discharge plateaus at approximately 1.5 V and 1.4 V/1.2 V (**Figure 4f**) are consistent with the electrochemical behavior observed in small-scale test cells (**Figure 4b**). This provides a feasible route for increasing the single cell capacity in the future.



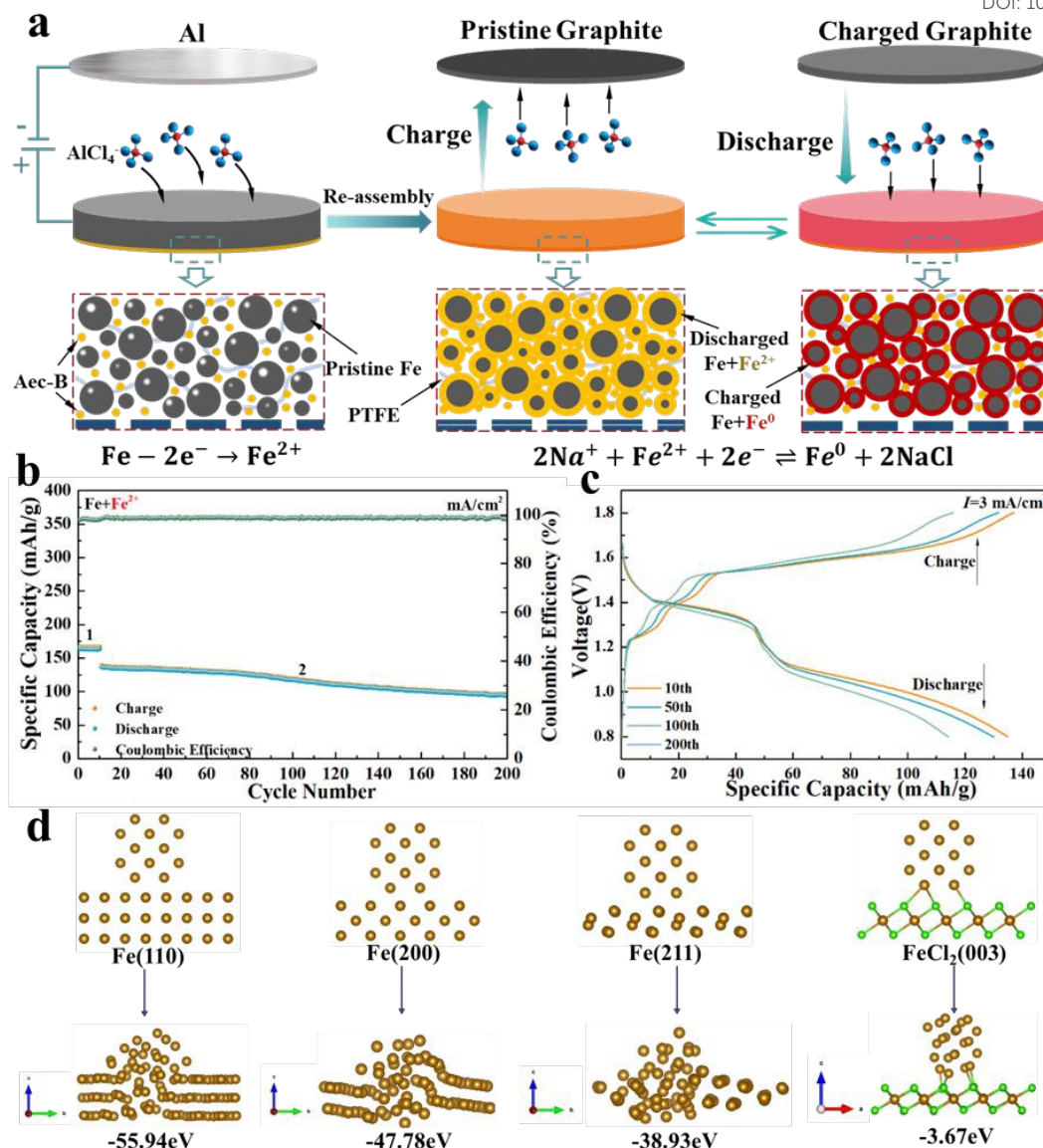
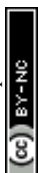


**Figure 5.** (a) Schematic of the electrochemical activation process of the 100 wt% nano-Fe powder electrode (Fe-CR-100) and electrode reaction mechanism in the reassembled full cell. (b-c) Cycling performance and voltage curves of the activated Fe-CR-100 electrode in Fe/FeCl<sub>2</sub>-graphite molten salt battery. (d) DFT calculation of iron cluster atoms on different material crystal planes.

To investigate the electrochemical activity of the nano-Fe interface in the oxidation reaction, we further examined the reversibility of an electrochemical pre-oxidized nano-Fe electrode in the Fe/FeCl<sub>2</sub>-graphite molten salt battery. In the



electrochemical oxidation reaction, Fe-CR-100 electrode and aluminum metal are used as the oxidizing anode and cathode, respectively. As shown in **Figure 5a**, the initial interface oxidation is performed in the Al-Fe half-cell by galvanostatic anodic polarization at  $1 \text{ mA cm}^{-2}$  (potential curve in **Figure S12**). During this galvanostatic anodic, the nano-Fe surface undergoes  $\text{Fe} \rightarrow \text{Fe}^{2+}$  oxidation, forming  $\text{FeCl}_2$  and the solid oxide film containing  $\text{Fe}^{2+}$ <sup>15</sup>. The Fe/ $\text{FeCl}_2$ -graphite battery is then reassembled by using the electrochemical oxidized Fe-CR-100 electrode. The performance is shown in **Figure 5b-c**. The oxidized negative electrode delivers an initial capacity of  $163.63 \text{ mAh g}^{-1}$  at  $1 \text{ mA cm}^{-2}$ . When the current density is increased to  $2 \text{ mA cm}^{-2}$ , the specific capacity of  $136.98 \text{ mAh g}^{-1}$  is maintained, confirming that the  $\text{Fe}^{2+}$  formed during pre-oxidation can be reversibly reduced upon charging and that the nano-Fe particle interface is gradually activated as the dominant electroactive interface. The corresponding voltage curves (**Figure 5c**) show charge plateaus at  $\sim 1.33 \text{ V}$ ,  $1.39 \text{ V}$  and  $1.54 \text{ V}$ , and discharge plateaus at  $\sim 1.41 \text{ V}$  and  $1.12 \text{ V}$ , which are nearly identical to those of the Fe- $\text{FeCl}_2$ -CR-60 electrode (**Figure 4b**). This indicates that the  $\text{FeCl}_2$  formed on the nano-Fe surface after pre-oxidation is reduced during the first charge, and the activated nano-Fe interface thereafter exhibits the same electrochemical behavior as that in the Fe- $\text{FeCl}_2$ -CR-60 electrode. After 200 cycles, the electrode retains a specific capacity of  $93.78 \text{ mAh g}^{-1}$ , demonstrating that redox reactions occurring at the pure nano-Fe interface possess superior reversibility compared to the pure  $\text{FeCl}_2$  electrode ( $\text{FeCl}_2$ -CR, **Figure S4**). This finding is consistent with our previous research, in which the  $\text{Fe}^{2+}$ -containing oxide film can form on the metallic Fe foam surface under



oxidative conditions, and the interfacial oxidized  $\text{Fe}^{2+}$  film exhibits excellent electrochemical reversibility in Fe/ $\text{FeCl}_2$ -graphite molten salt battery (The Fe/ $\text{Fe}^{2+}$  negative electrode prepared by electrochemical anodic electrolysis strategy, exhibits stabilized capacity of  $0.72 \text{ mAh/cm}^2$  after 7000 cycles at  $5 \text{ mA/cm}^2$ , with low polarization level about  $29 \text{ mV}$ )<sup>15</sup>. By simulating the oxidation atmosphere during electrode discharging, similar oxidation behavior was observed for the nano-Fe electrode. Therefore, the excellent reversibility and rate capability of the optimized Fe- $\text{FeCl}_2$ -CR-60 electrode are primarily attributed to the initial  $\text{FeCl}_2$  supply and the progressive activation of the nano-Fe particle interface, which gradually becomes the dominant region governing electrode capacity and electrochemical activity.

To understand the difference in nucleation stability of metallic  $\text{Fe}^0$  generated from the reduction of initial  $\text{FeCl}_2$ , DFT calculations are performed to compare the binding energies of  $\text{Fe}^0$  atomic clusters on different  $\text{FeCl}_2$  and Fe crystal planes according to the main crystal planes detectable in XRD testing (as shown in **Figure S13-S14**). As illustrated in **Figure 5d**, the binding energy (The detailed information is shown in **Figure S15-S18**) between  $\text{Fe}^0$  clusters and the main crystal planes of nano-Fe powder are all higher than that of the surface of  $\text{FeCl}_2$  under the same conditions. That is to say, compared to the  $\text{FeCl}_2$  material in the Fe- $\text{FeCl}_2$ -CR electrode, the crystal surface (110, 200 and 211) of nano-Fe powder is more likely to become the main nucleation interface of  $\text{Fe}^0$  clusters. In summary, the nano-Fe powder in the Fe- $\text{FeCl}_2$ -CR-60 electrode provides the Fe-ophilic nucleation interface for reduced  $\text{Fe}^0$ , while the  $\text{FeCl}_2$  serves as the initial oxidized active material to meet the assembly requirement of the fully



discharged Fe/FeCl<sub>2</sub>-graphite battery.

View Article Online  
DOI: 10.1039/D6SC03818B

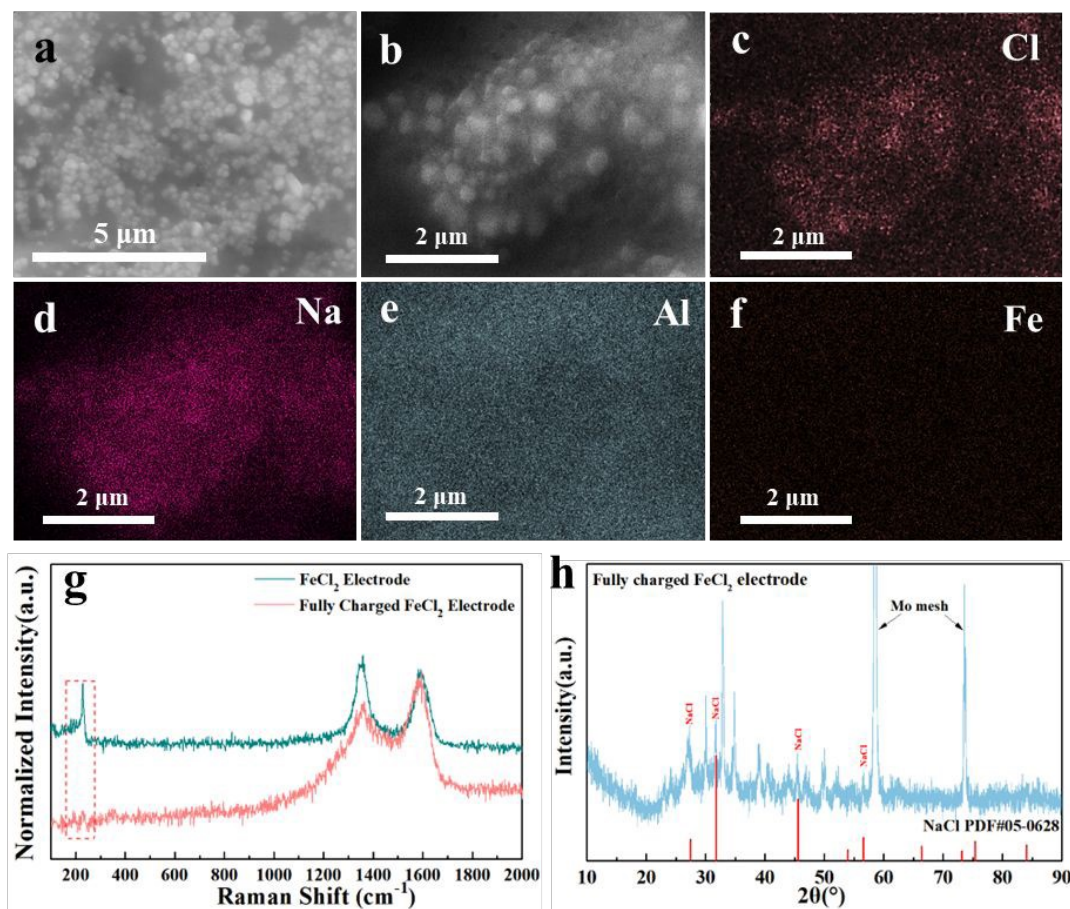


**Figure 6.** (a-b) SEM images of the fully charged pure FeCl<sub>2</sub>-CR electrode. (c-f) SEM-EDS elemental mappings of the pure FeCl<sub>2</sub>-CR electrode. (g) Raman spectra of the pristine and the fully-charged FeCl<sub>2</sub>-CR electrodes. (h) XRD pattern of the fully-charged FeCl<sub>2</sub>-CR electrode.

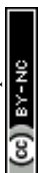
To elucidate the reaction mechanism of the dry-powder-calendered FeCl<sub>2</sub> electrode during charging, the reaction products and interfacial changes in the fully charged Fe/FeCl<sub>2</sub>-graphite molten salt battery are analyzed. As shown in **Figure 6a-f**, compared with the pristine surface of the calendered electrode, the charged FeCl<sub>2</sub> electrode shows uniform granular products (average particle size ~0.22 μm) adhering to the outer layer. SEM-EDS analysis reveals that these granules are primarily



composed of Cl and Na, confirming that the charging process involves the formation of NaCl solid phase. The Fe signal on the electrode surface is relatively low, likely because the electrolyte-derived membrane (containing Al and O) covers the underlying Fe<sup>0</sup> product. According to the Raman spectra in **Figure 6g**, the peaks at 1357 cm<sup>-1</sup> and 1591 cm<sup>-1</sup> in the pristine FeCl<sub>2</sub> electrode correspond to the D and G bands of the conductive agent acetylene black, while the signal at 229 cm<sup>-1</sup> is assigned to FeCl<sub>2</sub>. In contrast to the characteristic peaks of acetylene black, the peak near 229 cm<sup>-1</sup> disappears in the fully charged electrode, mainly because FeCl<sub>2</sub> is almost completely reduced to metallic Fe<sup>0</sup> during charging. Metallic elements do not exhibit Raman signals due to the absence of molecular vibrations. The XRD pattern in **Figure 6h** further confirms the phase transformation of the FeCl<sub>2</sub> electrode upon charging. The diffraction peaks at 58.81° and 73.62° are attributed to the molybdenum mesh current collector. Peaks at 27.29°, 31.75°, 45.51°, and 56.60° correspond to the (111), (200), (220), and (222) crystal planes of NaCl, respectively. The crystallization of NaCl particles on the electrode surface indicates that the electrolyte accessible FeCl<sub>2</sub> undergoes reduction during the charging process.

#### 4. Conclusions

In summary, the Fe-FeCl<sub>2</sub> contact interface is constructed for the Fe/FeCl<sub>2</sub> negative electrode via the solvent-free powder-calendering strategy. Here, nano-Fe powder mainly serves as the potential Fe-philic nucleation interface to induce the distribution of reduced Fe<sup>0</sup>, while FeCl<sub>2</sub> acts as the initial oxidation agent to meet the assembly requirement of the battery in a fully discharged state. Unlike the pure



interfacial oxidation ( $\text{Fe} \rightarrow \text{Fe}^{2+}$ ) in chemical or electrochemical chlorination, the repeated dry-powder-calendering process provides sufficient contact between metallic Fe and  $\text{FeCl}_2$ , which favors the nucleation and growth of reduced  $\text{Fe}^0$  on the nano-Fe interface. The Fe- $\text{FeCl}_2$ -CR-60 electrode exhibits low redox overpotential (0.09 V) and pulse DC internal resistance (1.74  $\Omega$ ) compared with the  $\text{FeCl}_2$ -CR electrode. In the Fe/ $\text{FeCl}_2$ -graphite molten salt battery, the Fe- $\text{FeCl}_2$ -CR-60 electrode delivers a specific capacity of 162.6 mAh  $\text{g}^{-1}$  at 3 mA  $\text{cm}^{-2}$  and retains 93% of its capacity after 200 cycles, with the active-material utilization increasing to 27.15%. DFT calculations reveal that the Fe (110) crystal plane in the Fe- $\text{FeCl}_2$  hetero-interface possesses the highest binding energy (-55.94 eV), which facilitates the nucleation and growth of reduced  $\text{Fe}^0$  clusters. Pre-oxidation experiments on the Fe-CR-100 electrode suggest that the surface of nano-Fe powder can be activated during electrochemical oxidation, thereby improving the electrode's electrochemical reversibility and ultimately leading to the stable, reversible electrochemical interface. Corresponding room-temperature self-discharge tests and capacity-expanded experiments further confirm the electrochemical reaction stability of the calendered Fe- $\text{FeCl}_2$ -CR electrode for Fe/ $\text{FeCl}_2$ -graphite molten salt battery.

### Author contributions

Wenlong Zhang: Conceptualization, Data curation, Formal analysis, Visualization  
Funding acquisition, Writing-original draft. Xiaohui Ning: Project administration,  
Resources, Funding acquisition, Supervision, Validation, Writing-review & editing.

### Conflicts of interest



There are no conflicts to declare.

## Acknowledgements

This work is supported by the National Natural Science Foundation of China (52504339, 92372205, 51874228) and Natural Science Foundation of Shaanxi Province, China (2020JM-068). The author gratefully acknowledges the support of K. C. Wong Education Foundation.

## References

1. C. Chen, C.-S. Lee and Y. Tang, *Nano-Micro Letters*, 2023, 15, 121.
2. Q. Pang, J. Meng, S. Gupta, X. Hong, C. Y. Kwok, J. Zhao, Y. Jin, L. Xu, O. Karahan, Z. Wang, S. Toll, L. Mai, L. F. Nazar, M. Balasubramanian, B. Narayanan and D. R. Sadoway, *Nature*, 2022, 608, 704-711.
3. L. Wang, Q. Li, Y. Wang, Y. Li, Z. Chen, L. Jiang and B. Tang, *Energy*, 2024, 309, 133140.
4. Y. Li, Y. Wang, Z. Chen, Q. Li, J. Du, J. Chai, L. Wang, Y. Rui, L. Jiang and B. Tang, *Chemical Engineering Journal*, 2023, 476, 146577.
5. Y. Wang, Y. Li, J. Chai, Q. Li, J. Du, Y. Rui, B. Tang and L. Jiang, *Chemical Engineering Journal*, 2024, 481, 148485.
6. L. Jiang, F. Liang, Z. Zhang, D. Wu, J. Chai, T. Luo, N. Han, W. Zhang, Y. Rui and B. Tang, *Chemical Engineering Journal*, 2022, 433, 133568.
7. X. Ning, S. Phadke, B. Chung, H. Yin, P. Burke and D. R. Sadoway, *Journal of Power Sources*, 2015, 275, 370-376.
8. H. Wang and C. Peng, *Sustainable Energy & Fuels*, 2023, 7, 330-354.
9. S. J. Percival, A. M. Maraschky, M. L. Meyerson, M. A. Stalcup, A. S. Peretti, L. J. Small and E. D. Spoeke, *Industrial & Engineering Chemistry Research*, 2025, 64, 22714-22723.
10. M.-C. Lin, M. Gong, B. Lu, Y. Wu, D.-Y. Wang, M. Guan, M. Angell, C. Chen, J. Yang, B.-J. Hwang and H. Dai, *Nature*, 2015, 520, 324-328.



11. J. Tu, J. Wang, H. Zhu and S. Jiao, *Journal of Alloys and Compounds*, 2020, 821, 153285. View Article Online  
DOI: 10.1039/D6SC03818B
12. T. Dai, L. Yang, X. Ning, D. Zhang, R. L. Narayan, J. Li and Z. Shan, *Energy Storage Materials*, 2020, 25, 801-810.
13. G. Li, X. Lu, J. Y. Kim, V. V. Viswanathan, K. D. Meinhardt, M. H. Engelhard and V. L. Sprenkle, *Advanced Energy Materials*, 2015, 5, 1500357.
14. G. Feng, Z. Liu, J. Holoubek, L. C. Greenburg, G. Zhang, Y. Li, X. Guan, Y. Cui, P. Zhang, A. Brest, X. Zheng and Y. Cui, *Nature Communications*, 2025, 16, 11055.
15. W. Zhang, H. Li and X. Ning, *ACS Applied Materials & Interfaces*, 2024, 16, 30545-30555.
16. H. Yang, F. Wu, W. Liu, X. Wang, Y. Bai and C. Wu, *Energy Storage Materials*, 2022, 51, 435-442.
17. W. Zhang, H. Li, H. Zhou and X. Ning, *Journal of Power Sources*, 2024, 593, 233958.
18. G. Kresse and J. Furthmüller, *Computational Materials Science*, 1996, 6, 15-50.
19. G. Kresse and J. Furthmüller, *Physical Review B*, 1996, 54, 11169-11186.
20. J. P. Perdew, K. Burke and M. Ernzerhof, *Physical Review Letters*, 1996, 77, 3865-3868.
21. G. Kresse and D. Joubert, *Physical Review B*, 1999, 59, 1758-1775.
22. P. E. Blöchl, *Physical Review B*, 1994, 50, 17953-17979.
23. S. Grimme, J. Antony, S. Ehrlich and H. Krieg, *The Journal of Chemical Physics*, 2010, 132, 154104.
24. J. Hong, J. Yoon, J.-W. Park, Y.-C. Ha, J. Lee and I. Hwang, *Journal of Power Sources*, 2025, 655, 237925.
25. B. G. Meyer, G. Matthews, R. Scales, N. C. Mitchell, E. Darnbrough, R. A. House, D. E. J. Armstrong and P. S. Grant, *ACS Materials Letters*, 2025, 7, 3444-3451.
26. Y. Song, S. Jiao, J. Tu, J. Wang, Y. Liu, H. Jiao, X. Mao, Z. Guo and D. J. Fray, *Journal of Materials Chemistry A*, 2017, 5, 1282-1291.



27. J. Tu, W.-L. Song, H. Lei, Z. Yu, L.-L. Chen, M. Wang and S. Jiao, *Chemical Reviews*, 2021, 121, 4903-4961.
28. X. Ao, Z. Wen, Y. Hu, T. Wu, X. Wu and Q. He, *Journal of Power Sources*, 2017, 340, 411-418.
29. G. Li, X. Lu, J. Y. Kim, M. H. Engelhard, J. P. Lemmon and V. L. Sprenkle, *Journal of Power Sources*, 2014, 272, 398-403.
30. X. Zhan, M. E. Bowden, X. Lu, J. F. Bonnett, T. Lemmon, D. M. Reed, V. L. Sprenkle and G. Li, *Advanced Energy Materials*, 2020, 10, 1903472.
31. M. M. Li, X. Zhan, E. Polikarpov, N. L. Canfield, M. H. Engelhard, J. M. Weller, D. M. Reed, V. L. Sprenkle and G. Li, *Cell Reports Physical Science*, 2022, 3, 100821.



The authors declare that the data supporting the findings of this study are available within the paper and its Supplementary Information files. Should any raw data files be needed in another format they are available from the corresponding author upon reasonable request. Source data are provided with this paper.

